

Prediction of the future urban heat island intensity and distribution based on landscape composition and configuration: A case study in Hangzhou

Chuhui Shen ^a, Hao Hou ^{a,b,*}, Yaoyao Zheng ^a, Yuji Murayama ^c, Ruci Wang ^c, Tangao Hu ^{a,b}

^a Institute of Remote Sensing and Earth Sciences, Hangzhou Normal University, Yuhangtang Road No. 2318, Hangzhou 311121, China

^b Zhejiang Provincial Key Laboratory of Urban Wetlands and Regional Change, Hangzhou Normal University, Yuhangtang Road No. 2318, Hangzhou 311121, China

^c Faculty of Life and Environmental Science, University of Tsukuba, 1-1-1 Tennodai, Tsukuba, Ibaraki 305-8572, Japan



ARTICLE INFO

Keywords:

Future simulation
Land surface temperature
Landscape pattern
Surface urban heat island intensity

ABSTRACT

During rapid urbanization, global land use and land cover change drastically, leading to increasingly severe problems in the urban environment. Among them, the urban heat island effect has attracted much attention owing to its magnification effect on climate change and its negative role in urban livability and sustainable development. In this context, predicting the future surface urban heat island intensity (SUHII) and distribution is important in dealing with the urban thermal environment. In this study, we conducted a prediction of SUHII using a random forest model based on future landscape patterns. According to the results, the built-up area is expected to grow to 3740.67 km², and the non-forest green space (GS2) is estimated to decrease by 1130.96 km² by 2030. In the context of urban expansion, the area with SUHII of higher than 5 °C will increase significantly, showing a more concentrated spatial distribution, while the region with SUHII of below -2.5 °C will decrease in coverage. In addition, our results showed that the scattered built-up areas and GS1, as well as concentrated GS2, will contribute to reducing SUHII. The results are expected to help policymakers and urban planners to design reasonable measures for achieving sustainable urban development.

1. Introduction

As the fundamental place of human activity, cities are the leading carriers of modern economic and technical development (Henderson, 2010). The future of humankind depends on the sustainable development of cities (Sun et al., 2020). In recent decades, the world has experienced large-scale and rapid urbanization (Ezimand et al., 2021). Over the next decade, the world will further urbanise, with the urbanization rate increasing from 56.2% in 2020 to 60.4% in 2030 (United Nations, 2020). To satisfy the rapid urbanization, a large quantity of natural surfaces has been replaced by impervious surfaces (Deng & Wu, 2013; Fu & Weng, 2016), thus, promoting significant changes in land use and land cover (LULC) in urban and rural regions (Du et al., 2016; Meng et al., 2018; Unal Cilek and Cilek, 2021). The variation in LULC leads to a decline in the urban ecosystem service function (Kindu et al., 2016), which inevitably poses increasingly serious environmental problems (Kang et al., 2019; Yin et al., 2018), especially in developing countries such as India and China (Das & Das, 2019; Sharma et al., 2020).

LULC change is a vital inducement and result of global change;

exploring the dynamic changes in the land system is the key link to understanding the environmental effects of human activities (Foley et al., 2005; Song et al., 2018). With the deep development of global change research, LULC change analysis has gradually become the core component of global environmental change research. By analyzing the satellite data of global land dynamic change from 1982 to 2016, Song et al. (2018) found that global land use change showed regional dominance; that is, montane systems have gained tree cover and many arid and semi-arid ecosystems (e.g., Australia, China, and the US) have lost vegetation cover. Due to the unprecedented expansion of anthropogenic LULC changes and the reduction of natural and semi-natural habitats, Yohannes et al. (2021) found that 35.3% of the habitat quality in Ethiopia decreased from 1972 to 2017. In addition, LULC change increases the frequency of floods, which are more likely to occur in residential areas than in grasslands and barren land since built-up areas inhibit surface runoff (Rahman et al., 2021). The study conducted in Australia found that urban heat island intensity showed a uniform increasing trend with an $\sim 1.20 \pm 0.20$ °C increment, along with the built-up land expansion of 14.93% from 2001 to 2014 (Mohammad Harmay et al., 2021). Meanwhile, LULC change is one of the important

* Correspondence author at: Institute of Remote Sensing and Earth Sciences, Hangzhou Normal University, Yuhangtang Road No. 2318, Hangzhou 311121, China.
E-mail address: houhao@hznu.edu.cn (H. Hou).

factors leading to global warming, which is predicted to cause 0.27 °C mean surface warming per century (Kalnay & Cai, 2003). Among various eco-environmental problems the urban heat island (UHI) effect has become a source of concern because of its negative role in urban livability (Tian et al., 2021) and sustainable development (Guo et al., 2020). The UHI effect, which refers to the phenomenon that cities suffer higher temperatures than suburbs (Manoli et al., 2019), is one of the most significant effects of human activity on local climate represented by urbanization (Grimm et al., 2008). The main consequences of UHIs include exacerbation of environmental pollution (Li et al., 2018), aggravated resource consumption (Shi et al., 2021), and threat to human health (Zhang, 2020). Systematic and scientific UHI research should be conducted to identify effective mitigation strategies and build a sustainable urban landscape.

Many factors affect UHI, including urban form (H. Liu et al., 2021), LULC change (Bokaie et al., 2016; Fu & Weng, 2016), climate change (Zhao et al., 2014), and anthropogenic heat emissions (Wang et al., 2021). Among them, LULC change directly corresponds to ecological processes, such as surface solar radiation absorption (Pal & Ziaul, 2017) and evapotranspiration (Fitria et al., 2019), thus affecting the surface heat transfer and determining the intensity of the UHI. The variation in landscape patterns reflects how human beings change land use (C. Liu et al., 2021). Land surface temperature (LST) is one of the most important indicators of surface UHI (SUHI) (Yang et al., 2020). Based on historical remote sensing data, many scholars have investigated the coupling relationship between LULC and LST from landscape patterns (Estoque et al., 2017; Peng et al., 2016; Wang et al., 2020) and have reached a common understanding. In general, the highest LST is primarily concentrated in built-up areas (Wang & Murayama, 2020), while large lakes and forests have lower LST due to cooling effects (Zhao et al., 2020; Zheng et al., 2021). In addition, adjusting the spatial configuration of various types of landscapes is an effective way to reduce LST (Hou & Estoque, 2020). However, previous studies mostly focused on the correlation analysis between landscape patterns and LST in the time domain, and few studies predicted the corresponding SUHII pattern based on future LULC changes. Compared with proposing the response plan after the arrival of high temperatures, predicting the future SUHII in advance and formulating a corresponding plan can alleviate the SUHI more effectively.

Future landscape prediction is one of the hotspots of current research. Many spatial prediction models and algorithms have been proposed and applied to the simulation of future landscapes, such as CA-Markov, artificial neural network (ANN), and CLUE-S (Hou et al., 2019; Islam et al., 2018). In recent years, some researchers have attempted to forecast future LST using these spatial prediction models and algorithms. However, in these studies, LST was predicted based solely on historical LST and LULC datasets, regardless of the impact of future LULC changes on local LST (Esha & Rahman, 2021; Kafy et al., 2020). This leads to low reliability and accuracy of the prediction results. To overcome this limitation, on the basis of simulating land use change in 2033 by using CA-Markov and ANN models, Nadizadeh Shorabeh et al. (2020) predicted the SUHII. Some scholars also began to introduce spectral indices, such as normalized difference vegetation index (NDVI), normalized differences built-up index (NDBI), and urban index (UI), into the prediction model (Feng et al., 2018; Khan et al., 2022; Ullah et al., 2019). For instance, Wang et al. (2020) estimated the future distribution of LST in Nanjing in 2030 and 2050 based on the relationship between LULC, NDVI, and LST. In the prediction study conducted by Mushore et al. (2017) in Harare, UI was selected as a predictor of LST, and they predicted that the area with a LST of 18–28 °C will decrease between 2015 and 2040, while the area with a LST of 36–45 °C will increase from 42.5 to 58% of the city. However, due to the limited LULC information reflected by the spectral index, these research results cannot directly guide local governors to make urban landscape reorganizing plans to alleviate the SUHI effect. Based on the historical dataset, Chen et al. (2022) found that the landscape indices also contribute significantly to LST

prediction. Compared with the spectral index, the landscape index can better quantify the composition and configuration of landscape patterns (Peng et al., 2016), which is of great significance for guiding urban planning to adapt to climate change. In conclusion, there is a knowledge gap in the SUHI prediction research. The previous prediction methods also need to be improved in the perspectives of parameters and modelling algorithms. Thus, it is necessary to carry out future SUHI prediction research based on landscape patterns expressed by composition and configuration indices with different modelling methods.

Hangzhou, the capital city of Zhejiang Province, has experienced rapid urbanization over the past two decades. Owing to the large-scale urban expansion, the landscape of Hangzhou has undergone significant changes (Hou et al., 2019; Lin et al., 2018). Coupled with the influence of a huge urban population and intensive human activities, the SUHI effect in Hangzhou is becoming increasingly serious (Tian et al., 2021). Hangzhou's livability has been challenged. With the continuous advancement of China's ecological civilisation construction, the SUHI has increasingly attracted attention. As a typical city in China in the perspective of rapid urbanization, the study of Hangzhou's SUHI will provide an essential reference for other fast-growing cities.

In light of the above considerations, the overall aim of this study is to project the SUHI distribution and intensity of Hangzhou in 2030 based on future landscape patterns. To achieve the main purpose, our sub-objectives included: (1) to explore the spatiotemporal patterns of LULC and LST in Hangzhou from 2000 to 2020; (2) to determine the optimal model and spatial scale for predicting SUHII; and (3) to simulate future SUHII patterns in 2030.

2. Materials and methods

2.1. Study area

Hangzhou (29°11'N–30°34'N, 118°20'E–120°37'E) is situated on the southern edge of the Yangtze River Delta, on the northern bank of the Qiantang River. As the political, economic, and cultural center of Zhejiang Province, Hangzhou has experienced rapid urbanization after the Reform and Open Door Policy in 1978, especially in the past two decades. According to statistics, Hangzhou's urbanization ratio, which measures the percentage of the urban population, increased from 58.64% in 2000 to 83.29% in 2020 (Hangzhou Municipal Government, 2021). By 2020, Hangzhou's total gross domestic product reached 1610.6 billion yuan, with an increase of 3.9% over the previous year and ranking 5th in the country (Hangzhou Municipal Bureau of Statistics, 2021). Known as a paradise on earth, Hangzhou has been a culture, heritage, and tourism hotspot. Hangzhou is characterised by a subtropical zone and has a typical monsoon climate with four distinct seasons (Lu et al., 2021), including hot and humid summers and cold and dry winters. In this study, to avoid the influence of changes in administrative boundaries over time, a landscape with a radius of 50 km from the city center (Wulin Square) was chosen as the study area (Fig. 1).

2.2. Data collection and pre-processing

2.2.1. Landsat images for SUHI intensity calculation

In 2021, USGS launched a new Landsat Collection 2 Level 2 dataset on the Google Earth Engine (GEE) platform, which contains scene-based global Level-2 surface reflectance and surface temperature science products (<https://www.usgs.gov/landsat-missions/landsat-collection-2-level-2-science-products>). In this study, we selected images with less than 20% cloud cover from June to September in 2000, 2010, and 2020 (Table 1). To maintain high image quality and provide accurate information of LST, the images of adjacent years were also taken into account in the process of data collection. The Quality Assessment (QA) bands generated from the C Function of Mask (CFMask) algorithm were used in all products to filter out further low-quality image pixels contaminated by clouds and cloud shadows. Finally, the quality-

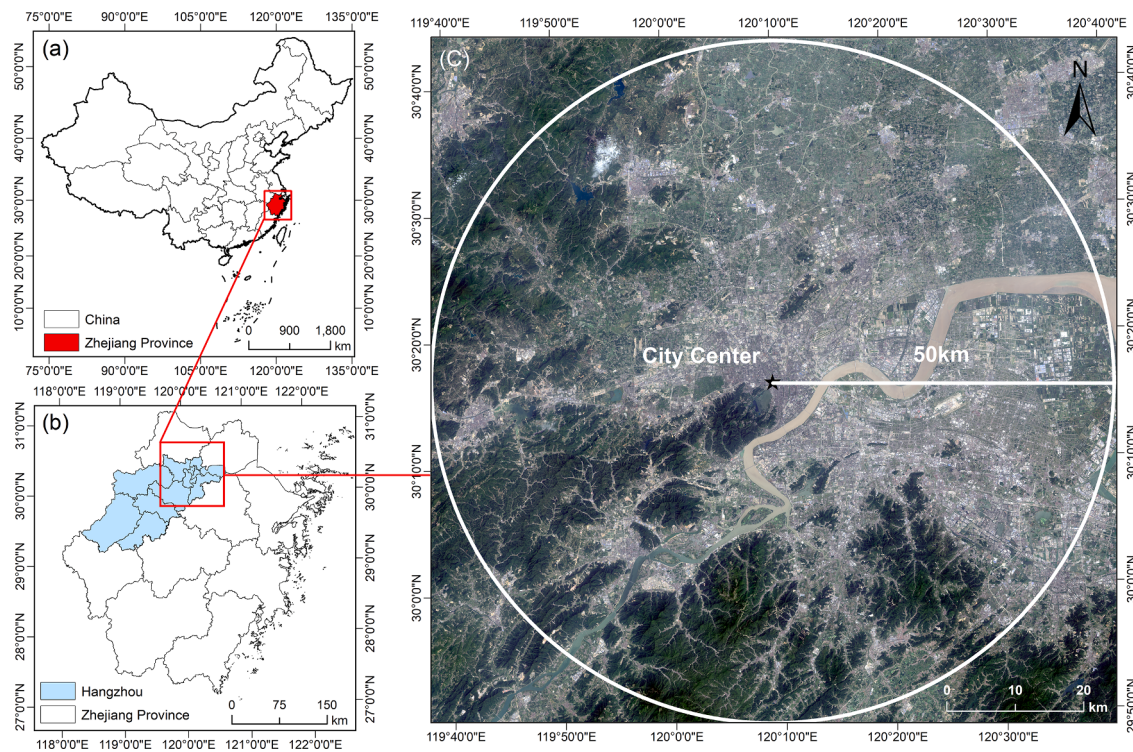


Fig. 1. Location of the study area: (a) Map of China; (b) Map of Zhejiang Province; and (c) Landsat-8 Operational Land Imager (OLI)/Thermal Infrared Sensor (TIRS) image of the study area, which was displayed in true color composite (Red-Band 4; Green-Band 3; Blue-Band 2).

controlled dataset was used to generate the mean LST images.

2.2.2. Landsat images for LULC classification

In this study, three cloud-free (<10%) Landsat images obtained from the United States Geological Survey (USGS) (<https://earthexplorer.usgs.gov/>) were used to derive the changes in LULC in the study area from 2000 to 2020. To avoid the consequences of seasonal variation, all downloaded images were collected from June to September (see Table 1).

To enhance the quality of the images and reduce the interference of atmosphere and light on the surface reflection, the process of radiometric calibration and fast line-of-sight atmospheric analysis of spectral hypercubes (FLAASH) atmospheric corrections were completed using the ENVI 5.3 software package. During data pre-processing, the digital number (DN) of the multispectral bands was validated as reflectance, while the DN of the thermal band was validated as radiance.

2.2.3. Driving factors dataset

The LULC change results from the comprehensive effects of natural and human factors. Therefore, five socio-economic factors were considered as additional modelling parameters: distance to the city center, railways, highways, main roads, and rivers. These vector data were obtained by vectorization of historical images. Then, the "Euclidean distance" tool in ArcGIS was used to generate distance maps. Two natural factors, the digital elevation model (DEM) and slope, were also included in the modelling process. DEM data were derived from the USGS, and the slope was extracted from DEM.

2.3. Workflow

This study aims to predict future landscape patterns and SUHII distribution. In order to accomplish this objective, the workflow was designed (Fig. 2) with five main procedures including: (1) SUHII calculation and LULC classification based on Landsat multi-temporal images; (2) landscape index calculation; (3) development of SUHII

prediction models based on stepwise multiple linear regression (SMLR) and random forest (RF) algorithms; (4) land cover simulation based on LULC maps and driving factors using the land change modeler (LCM); and (5) future SUHII prediction based on a prediction model and land cover simulation.

2.4. Calculation of SUHII

SUHII is an effective parameter to characterize SUHI effect (Peng et al., 2020; Wu et al., 2022). We used the following formula to calculate SUHII:

$$SUHII = T - T_{rural} \quad (1)$$

where T refers to the LST of each pixel, and T_{rural} represents the mean LST of the rural pixel. In this study, according to the LULC classification map, all areas except built-up and water were defined as rural.

2.5. LULC classification and accuracy assessment

The support vector machine (SVM) is an algorithm of machine learning which was widely used in image classification. Compared with other classification algorithms (e.g., minimum distance, maximum likelihood classifier, and Mahalanobis distance), it has the advantages of not interfering with the likelihood function and having the minimum training data requirements (Tariq & Shu, 2020). Furthermore, in our pre-experiment, SVM has higher accuracy than other classification methods, so we selected SVM as the LULC classification method in this study. Radial basis function was selected as the kernel type; gamma in kernel function was set to 1.00; and penalty parameter was set to 100.00. Based on the purpose of this study, five major land cover types were extracted from the Landsat images: built-up, forest (GS1), water, non-forest green space (GS2), and bare. Detailed descriptions of these categories are provided in Table S1. The accuracy verification was completed by creating 500 random points in each classified LULC map and comparing them with the real historical Google Earth image. In

Table 1

Data used in this study and their associated information.

Data Type	Time	Resolution	Source	Usage
Landsat Collection 2 Level 2 dataset	2000/06/13, 2000/07/07,	30 m	USGS	SUHII calculation
	2000/07/31, 2000/08/08,			Modelling variable
	2000/09/17, 2009/06/06,			
	2009/08/25, 2009/09/10,			
	2010/08/12, 2011/07/30,			
	2011/09/16, 2019/08/21,			
	2020/08/23, 2020/09/08,			
	2021/06/23, 2021/09/27			
Landsat-5 TM	2000/09/17	30 m		LULC classification
		Modelling variable		
Landsat-5 TM	2010/08/12	30 m		LULC classification
		Modelling variable		
Landsat-8 OLI/TIRS	2020/09/08	30 m		LULC classification
		Modelling variable		
DEM	-	90 m		Extract slope
River	2000, 2010, 2020	Vector	Vectorization	Modelling variable
Railway	2000, 2010, 2020	Vector	Vectorization	Modelling variable
Highway	2000, 2010, 2020	Vector	Vectorization	Modelling variable
Main roads	2000, 2010, 2020	Vector	Vectorization	Modelling variable
City center	-	Vector	Fieldwork	Modelling variable

2000, 2010, and 2020, the overall classification accuracies were 95%, 89.9%, and 86.4%, respectively.

2.6. Landscape metrics

Landscape indices can effectively reflect the information of landscape patterns from two aspects: composition and configuration (Wang et al., 2020). Based on LULC maps, referring to previous research results combined with the purpose of this study, five landscape metrics with basic landscape characteristics were selected (Table 2): the percentage of landscape (PLAND), aggregation index (AI), patch density (PD), largest patch index (LPI), and mean shape index (SHAPE_MN). The metrics for this study were chosen according to the following principles (Maimaitiyiming et al., 2014; Wu et al., 2014): (1) theoretically and practically important; (2) easily calculated and interpreted; (3) minimal redundancy. Landscape metrics were calculated by applying the uniform tile method in FRAGSTATS V4.2.1. The correlation between landscape patterns and LST is greatly affected by the spatial scale. As a result, three grids with different sizes, 510 m (17×17 pixels), 990 m (33×33 pixels), and 1500 m (50×50 pixels), were created for further analysis.

P_i = proportion of the landscape occupied by patch type (class) i; a_{ij} = area (m^2) of patch ij; A = total landscape area (m^2); g_{ii} = number of like adjacencies (joins) between pixels of patch type (class) i based on the single-count method; $\max(g_{ii})$ = maximum number of like adjacencies (joins) between pixels of patch type (class) i based on the single-count method; n_i = number of patches in the landscape of patch type (class) i; p_{ij} = perimeter (m) of patch ij.

2.7. Modelling future LULC using LCM

The land change modeller (LCM) embedded in Terrset is an integrated software for exploring the LULC patterns and projecting future LULC (Wang & Murayama, 2020). LCM integrates a multilayer perceptron ANN (MLP-ANN), Markov model, and soft and hard prediction model (Ansari & Golabi, 2019; Chanapathi & Thatikonda, 2020; Leta et al., 2021), which is an empirical parametric model. In this study, LCM was employed to simulate the LULC maps through the following three steps: (1) combining land use changes and seven other driving factors (i.e., DEM, slope, distance to the city center, rivers, railways, highways, and main roads) to create the transfer potential maps by MLP-ANN method; (2) generating a transition probability matrix using a Markov chain; and (3) simulating future LULC maps by using a hard prediction model.

Model Validation is necessary to prove the soundness of the results. In this study, figure-of-merit (FoM) was adopted as the accuracy indicator because it is superior to the Kappa coefficient in evaluating the accuracy of simulated changes (Liu et al., 2017). This index can be expressed by Eq. (2) (Pontius et al., 2008; Sloan & Pelletier, 2012):

$$FoM = \frac{H}{H + M + F} \times 100\% \quad (2)$$

where H, M, and F are the hits, misses, and false alarms, respectively.

Thus, before simulating the future LULC maps, the data for 2000 and 2010 were used to simulate the LULC map in 2020. Next, the simulated map was compared with the actual map for 2020 to calculate the FoM. The prediction of the 2030 LULC maps (based on the 2010 and 2020 maps) was later conducted when the accuracy was acceptable.

2.8. Development of SUHI prediction models

2.8.1. Stepwise multiple linear regression (SMLR) model

Based on the LULC and LST maps of the three periods, the multiple linear regression (MLR) model was adopted to examine the relationship between mean SUHII and driving factors at different scales. The dependent variable was the mean SUHII, and the independent variables included PLAND, PD, LPI, SHAPE_MN, AL, and DEM. The dependent and independent variables of three years (2000, 2010, and 2020) in the same grid size were summarised together as the sample group to acquire more accurate regression results. The MLR equation is given by Eq. (3) (Hogan et al., 1970):

$$Y = \beta_0 + \sum_{k=1}^n \beta_k X_k + \varepsilon \quad (3)$$

where n is the number of independent variables, β_0 is the intercept, β_k represents the regression coefficients, and ε represents the random error term.

The stepwise regression method was selected to ensure that the variables in the model were significant and there was no multicollinearity. The thresholds for variables entering and exiting models were set to $p \leq 0.050$ and $p \geq 0.100$, respectively. Furthermore, a variable is excluded once its variance inflation factor (VIF) value is equal to or larger than 7.5. Before the regression analysis, all variables were normalized to eliminate the dimension's influence.

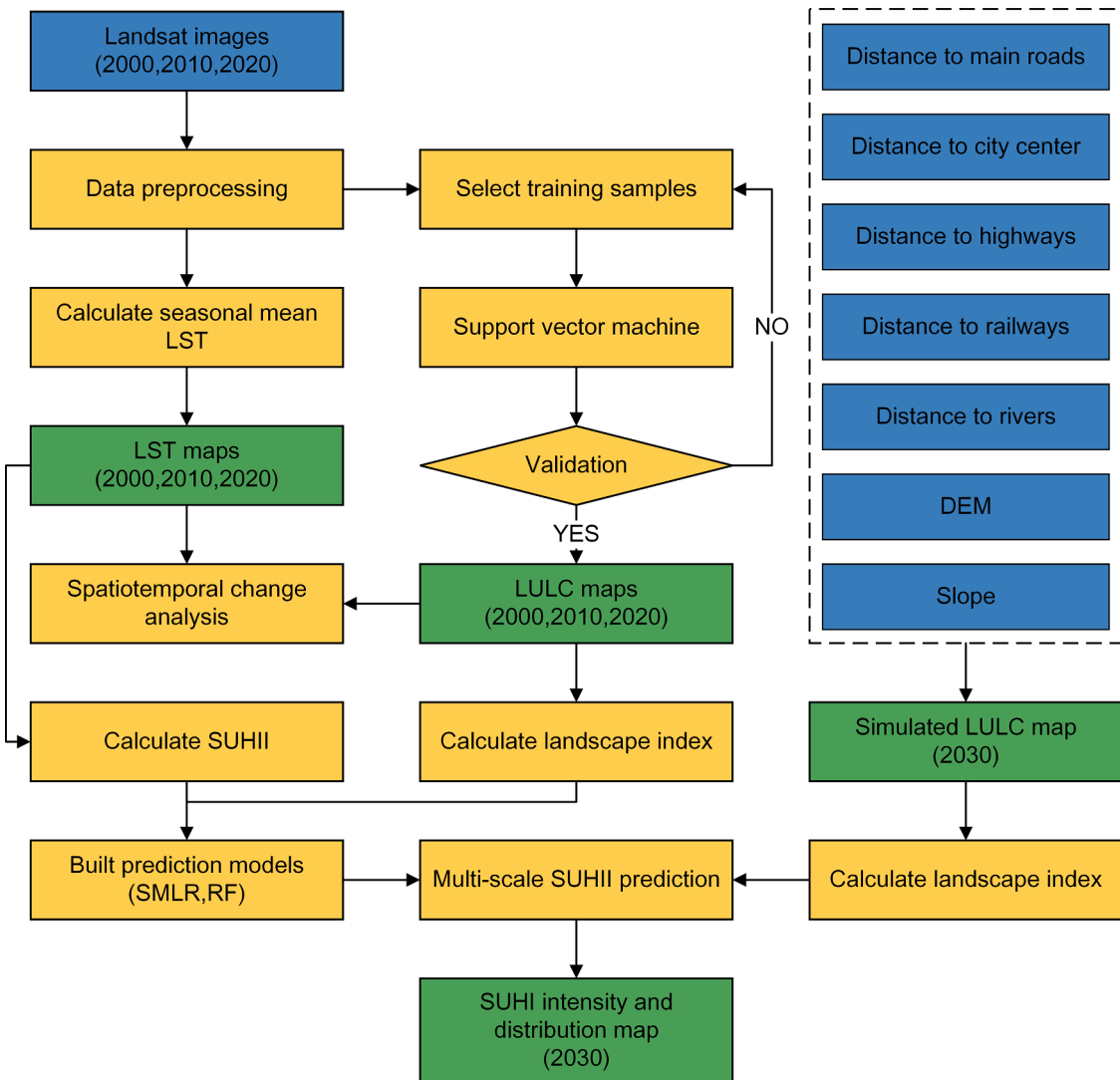


Fig. 2. Workflow of this study (blue, yellow, and green represent data, operations, and analysis results, respectively).

Table 2
Description of landscape metrics used in this study (McGarigal et al., 2012).

Metric (Abbreviation)	Equation(Unit)	Description
Percentage of landscape (PLAND)	$PLAND = P_i = \frac{\sum_{j=1}^n a_{ij}}{A} \times 100$	Landscape percentage of the corresponding patch.
Aggregation index (AI)	$AI = \left[\frac{g_{ii}}{\max(g_{ii})} \right] \times 100$	Degree of aggregation of the corresponding patches within an analysis unit.
Patch density (PD)	$PD = \frac{n_i}{A} \times 10^6$	The density of corresponding patches within an analysis unit.
Largest patch index (LPI)	$LPI = \frac{\max(a_{ij})}{A} \times 100$	The percentage of the landscape occupied by the largest patch.
Mean shape index (SHAPE_MN)	$SHAPE_MN = \frac{\sum_{j=1}^n 0.25 p_{ij}}{\sqrt{a_{ij}}}$	Average shape index of the corresponding patches within an analysis unit.

2.8.2. Random forest (RF) regression model

Considering the possible non-linear relationships between mean LST and its drivers, the widely used machine learning approach, the random forest model (Breiman, 2001), was also applied to model the SUHII based on landscape parameters. For forest parameter setting, we

considered ensembles of 100 trees, and each tree was grown on bootstrap samples of the data. The splitting of tree nodes was stopped if they contained less than five observations.

2.8.3. Model validation and SUHII prediction

To compare the prediction ability of the SMLR model and RF model, we took a validation and comparison process with the following steps: (1) randomly divide the dataset into two portions, 70% of the data for training purposes and the rest 30% for validation; (2) normalize the training set and keep the estimated coefficients (i.e., the maximum and minimum values), and the normalization can be applied to the test set using the coefficients; (3) calculating the coefficient of determination (R^2) and root mean square error (RMSE) using prediction dataset and observed dataset (derived from the testing dataset); (4) comparing the R^2 and RMSE of two models to determine the optimal SUHII prediction model.

When the model training was completed, the landscape index in 2030 was used as a new input to obtain the normalized predicted SUHII data. Then, the SUHII data was anti-normalization by using the average maximum and average minimum of historical LST data to obtain the predicted value of SUHII.

3. Results

3.1. Spatiotemporal changes of LULC in Hangzhou

Fig. 3 shows the LULC patterns of Hangzhou from 2000 to 2020. Spatially, the built-up area was concentrated in the city center and experienced large-scale outwards expansion; GS1 was the dominant land use type in the west and south; GS2 was primarily located in the east and northeast, exhibiting a decreasing trend; and the Qiantang River flows from the southwest to the east.

In terms of quantity (**Table 3**), the growth of the built-up area ranked first among all land use types: from 1781.30 km² in 2000 to 2148.07 km² in 2010, and 3110.37 km² in 2020, with an increase of 1329.07 km² over the past 20 years. Under such rapid growth, in 2020, the built-up area (31.11%) replaced GS2 (18.23%) as the second-largest land cover type in the study area after GS1 (42.10%). In contrast, GS2 exhibited the most significant loss. The area of GS2 decreased by 316.03 km² in the first decade, reaching 1325.83 km² of loss in the second decade. From 2000 to 2010, the GS1 area increased slightly (49.95 km²). However, from 2010 to 2020, GS1 experienced significant growth, with an area increasing to 4208.86 km². As the most stable land type, the area and proportion of water did not change significantly.

Fig. 4 shows that, over the past two decades, the transition from GS2 to built-up areas has been the main source of newly built areas, followed by GS1 and water to built-up areas. In the second decade, the occupation of GS2 by built-up areas became even more drastic. In addition, the increase in the GS1 area was mainly due to the loss of GS2.

3.2. Spatiotemporal patterns of LST in Hangzhou

All LST maps were normalized to compare LST distributions in different periods better. **Fig. 5** shows the spatiotemporal patterns of LST in 2000, 2010, and 2020. In the summer of 2000, the LST ranged between 5.86 and 63.76 °C, with an average value of 31.36 °C. In 2010, the LST ranged between 16.16 and 72.07 °C, with a mean value of 35.59 °C. In 2020, the LST ranged between 19.89 °C and 71.73 °C, with an average of 37.09 °C.

In 2000, there were two spatially independent areas with higher LST in the whole study area, which were located in the city center and the town in the southeast corner. In the first decade, the higher LST region located in the city center experienced outward expansion, primarily in the northeast and southeast. A number of originally scattered patches of high LST gradually expanded and merged. In the second decade, the region of higher LST continued to expand, accounting for nearly half of the study area. Except for the area around West Lake, the city center and its surrounding areas suffered high LST.

There was a similar distribution and trend between the LST and LULC, indicating that LST is closely related to LULC. High LST regions typically correspond to built-up areas. The average LST of built-up areas was 34.92, 40.54, and 41.36 °C in 2000, 2010, and 2020, respectively. Conversely, low LST areas were primarily water and the GS1 area. The mean LST of water was 29.75, 32.96, and 34.60 °C in 2000, 2010, and 2020, and those of GS1 were 29.56, 33.00, and 34.24 °C in 2000, 2010, and 2020, respectively.

3.3. Results of the prediction models

The optimal fitting equations for different grid sizes are shown in **Table 4**. The adjusted R² values of the three grid sizes were 0.725 (17 × 17), 0.755 (33 × 33), and 0.774 (50 × 50). The R² and adjusted R² of every model were greater than 0.7, indicating the good performance of the models. The significance level of all models was 5%.

In order to determine the optimal SUHI prediction scale and method, we used SMLR and RF methods to establish SUHI prediction models with grid sizes of 17 × 17, 33 × 33, and 50 × 50, respectively. **Fig. 6** shows the prediction ability of the six models. The performance of RF in predicting SUHI was significantly better than SMLR. As a result, we applied the RF model to predict future SUHI.

3.4. Future LULC distribution in 2030

To prove the accuracy and feasibility of the simulation model, the actual and the simulation maps of 2020 were compared. The FoM value was 15.58%, and the Kappa coefficient was 59.25%. The LULC distribution for 2030 is shown in **Fig. 7a**. By encroaching on other surrounding LULC (mainly GS2), the built-up area was predicted to grow by 2030. As a result of continuous expansion, previously scattered built-up patches were connected, thus, forming many complete and continuous patches. As the main land source of construction land expansion, the area of GS2 was predicted to be significantly reduced. **Fig. 7b** shows the number of mutual transitions between the five LULC types from 2020 to 2030. Following the law of the first two decades, it was estimated that by 2030, a total of 548.01 km² and 359.08 km² of GS2 would be converted into built-up and GS1 areas, respectively. The simulation results predicted that the built-up, GS1, water, GS2, and bare areas were expected to be 3740.67, 4363.22, 726.56, 1130.96, and 36.59 km², respectively. Compared with 2020, the built-up and GS1 area were predicted to increase by 6.30% and 1.54%, respectively.

3.5. Simulation results of SUHII in 2030

Considering the performance of RF models was significantly better

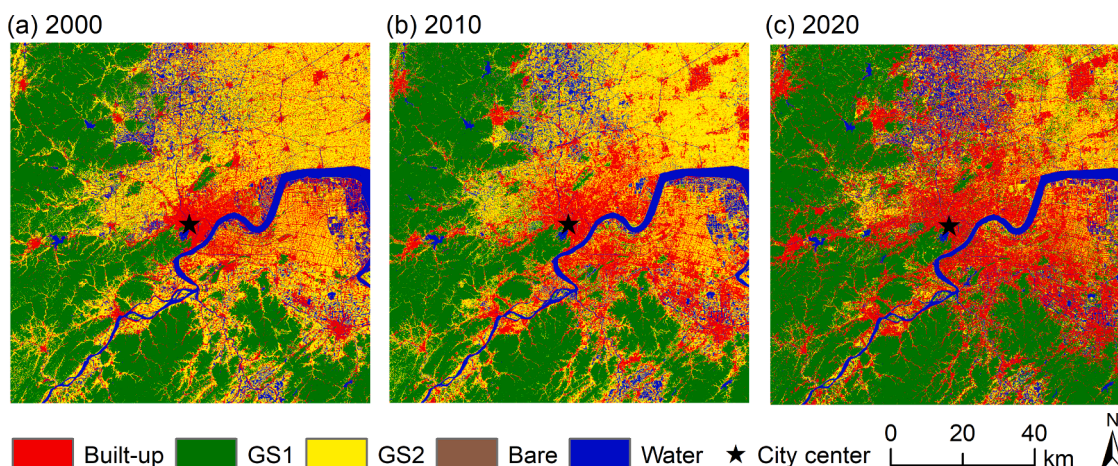


Fig. 3. LULC maps of Hangzhou in 2000, 2010, and 2020.

Table 3

Statistics of different land cover types from 2000 to 2020.

	2000		2010		2020	
	Area(km ²)	Percentage(%)	Area(km ²)	Percentage(%)	Area(km ²)	Percentage(%)
Built-up	1781.30	17.82	2148.07	21.49	3110.37	31.11
GS1	3726.14	37.27	3776.09	37.77	4208.86	42.10
GS2	3464.63	34.65	3148.60	31.49	1822.77	18.23
Bare	162.56	1.63	96.81	0.97	36.90	0.37
Water	863.37	8.64	828.42	8.29	819.11	8.19

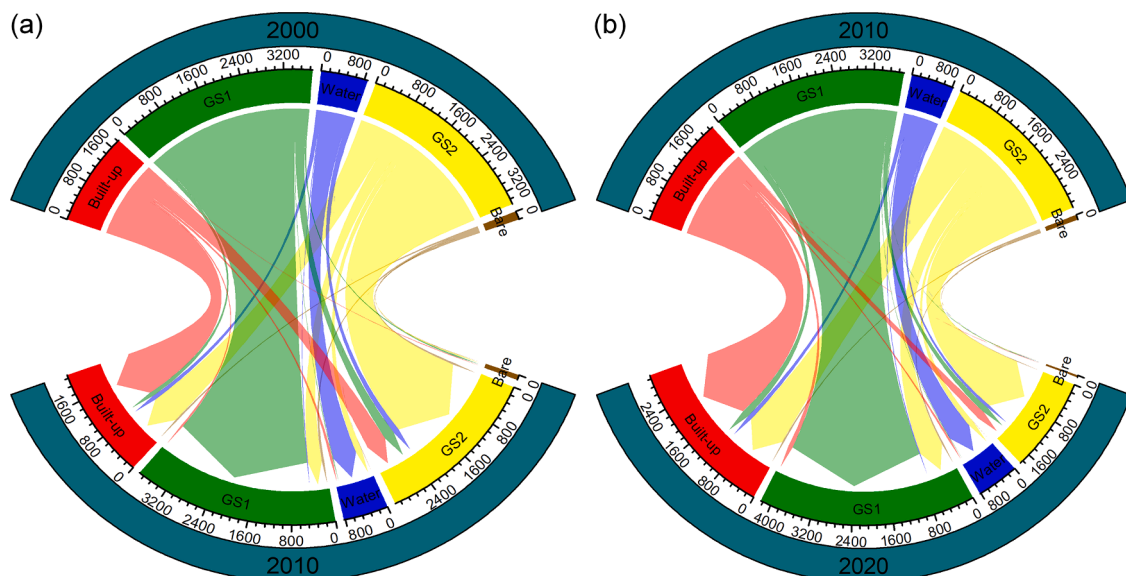
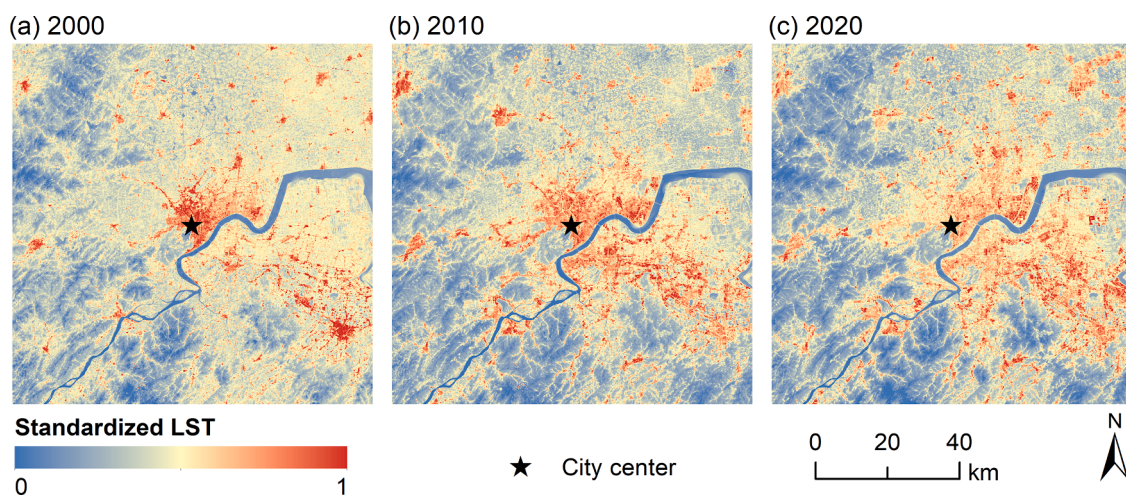
Fig. 4. LULC transitions between: (a) 2000–2010 and (b) 2010–2020 (in km²).

Fig. 5. LST maps of Hangzhou in 2000, 2010, and 2020.

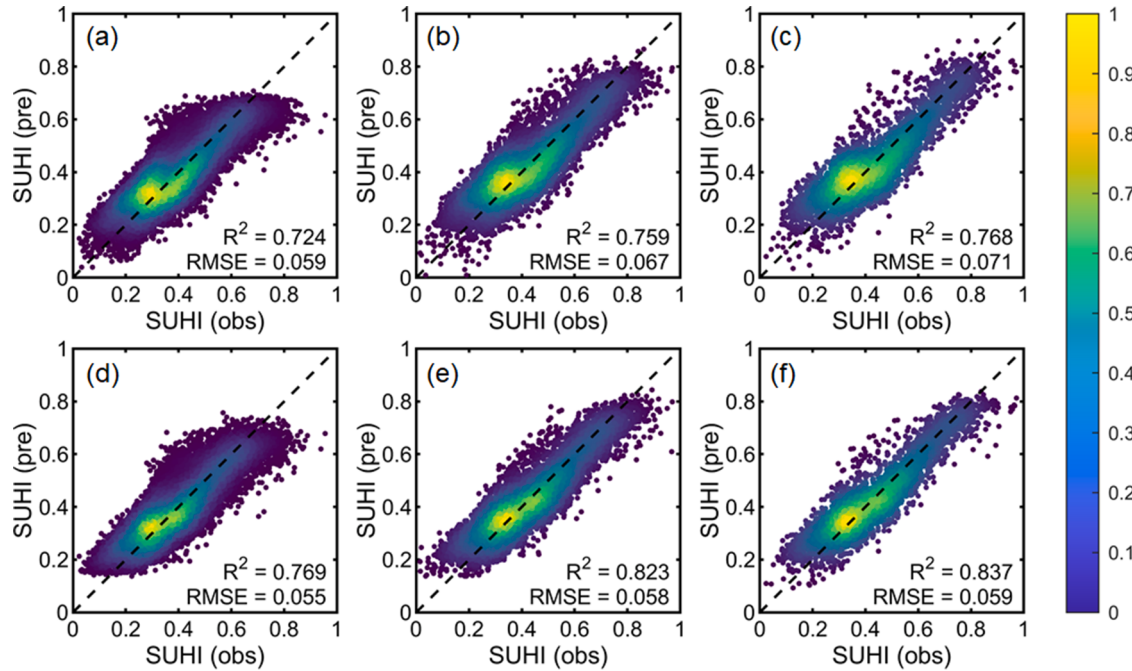
than SMLR models, the prediction of the SUHII was only based on three RF models. Based on the predicted SUHII data, the SUHII was classified and compared with the results in 2020 to reflect better the distribution and change of SUHII (Fig. 8). Table 5 shows the area statistics of each SUHII level. The area of SUHII below -2.5°C and the area of SUHII between $0\text{--}2.5^{\circ}\text{C}$ were supposed to decrease during 2020 and 2030. The $-2.5\text{--}0^{\circ}\text{C}$ class increased significantly due to the transformation from the $-5\text{--}-2.5^{\circ}\text{C}$ category and $0\text{--}2.5^{\circ}\text{C}$ category. In 2020, the study area was dominantly covered by SUHII in the $0\text{--}2.5^{\circ}\text{C}$ category, while this category was expected to experience a significant decline in 2030.

Compared with 2020, the area with SUHII greater than 5°C increased in 2030 with a more concentrated spatial distribution (Fig. 8). The projected growth areas of the three grids were 473.38 km^2 (17×17), 526.31 km^2 (33×33), and 603.00 km^2 (50×50), respectively (Table 5). For all transformations, the $0\text{--}2.5^{\circ}\text{C}$ and $2.5\text{--}5^{\circ}\text{C}$ categories were the main sources of growth in the area with SUHII greater than 5°C (Fig. 9b).

Table 4

Stepwise regression analysis results of different grid sizes.

Grid Size	Minimum (17×17)			Medium (33×33)			Maximum (50×50)		
	Variables	UC (Std. Error)	SC	VIF	UC (Std. Error)	SC	VIF	UC (Std. Error)	SC
(Constant)	0.291(0.002)	–	–	0.326(0.005)	–	–	0.341(0.009)	–	–
PLAND_Built-up	0.350(0.002)	0.707**	4.661	0.467(0.004)	0.733**	4.161	0.535(0.007)	0.758**	4.385
AI_Built-up	0.007(0.001)	0.019**	3.538	0.014(0.003)	0.023**	2.193	0.018(0.006)	0.022*	2.438
PD_Built-up	0.070(0.003)	0.067**	1.855	0.068(0.006)	0.058**	2.130	0.052(0.009)	0.044**	2.434
LPI_Built-up	–	–	–	–	–	–	–	–	–
SHAPE_MN_Built-up	0.036(0.004)	0.035**	3.449	–	–	–	-0.054(0.017)	-0.022*	1.935
PLAND_GS1	–	–	–	–	–	–	–	–	–
AI_GS1	0.034(0.001)	0.103**	5.678	0.052(0.003)	0.003**	0.121	0.068(0.005)	0.139**	4.76
PD_GS1	0.084(0.002)	0.078**	1.536	0.119(0.005)	0.121**	5.442	0.137(0.007)	0.129**	1.819
LPI_GS1	–	–	–	–	–	–	–	–	–
SHAPE_MN_GS1	0.032(0.003)	0.035**	2.449	0.040(0.011)	0.018**	2.079	0.074(0.016)	0.031**	1.84
PLAND_GS2	-0.020(0.002)	-0.043**	6.813	-0.020(0.005)	-0.035**	7.327	–	–	–
AI_GS2	-0.024(0.001)	-0.062**	4.123	-0.055(0.004)	-0.096**	3.755	-0.115(0.006)	-0.164**	3.185
PD_GS2	0.030(0.003)	0.027**	1.873	0.068(0.006)	0.061**	2.184	0.085(0.008)	0.079**	2.472
LPI_GS2	–	–	–	–	–	–	0.029(0.007)	0.042**	4.922
SHAPE_MN_GS2	0.063(0.003)	0.057**	2.449	0.131(0.010)	0.070**	2.347	0.183(0.021)	0.065**	2.163
PLAND_Bare	0.181(0.008)	0.057**	2.067	0.189(0.015)	0.069**	2.453	0.261(0.025)	0.089**	2.953
AI_Bare	0.015(0.001)	0.029**	2.021	0.016(0.002)	0.029**	1.819	0.022(0.004)	0.037**	1.659
PD_Bare	-0.142(0.004)	-0.106**	2.682	-0.219(0.008)	-0.156**	2.693	-0.313(0.014)	-0.200**	3.048
LPI_Bare	–	–	–	–	–	–	–	–	–
SHAPE_MN_Bare	0.073(0.003)	-0.086**	2.884	-0.099(0.005)	-0.095**	2.124	-0.095(0.007)	-0.088**	1.785
PLAND_Water	-0.089(0.002)	-0.127**	3.170	–	–	–	–	–	–
AI_Water	0.020(0.001)	0.059**	3.170	0.028(0.002)	0.064**	2.608	0.032(0.004)	0.059**	2.408
PD_Water	-0.127(0.003)	-0.114**	1.803	-0.212(0.006)	-0.172**	1.882	-0.254(0.009)	-0.202**	2.162
LPI_Water	–	–	–	-0.137(0.005)	-0.137**	2.596	-0.149(0.009)	-0.123**	2.136
SHAPE_MN_Water	-0.039(0.003)	-0.042**	3.502	-0.056(0.007)	-0.045**	2.929	-0.046(0.010)	-0.036**	2.668
DEM	-0.297(0.004)	-0.265**	2.906	-0.378(0.008)	-0.291**	3.662	-0.407(0.013)	-0.316**	4.130
R ²	0.725			0.755			0.774		
Adjusted R ²	0.725			0.755			0.774		

UC stands for unstandardized coefficient; SC stands for standardized coefficient. * $p < 0.01$; ** $p < 0.001$.**Fig. 6.** Model performance of SMLR and RF: (a)–(c) are the SMLR model results of the three grid scales (17×17 , 33×33 , and 50×50); and (d)–(f) are the RF model results of the three grid scales.

4. Discussion

In the past two decades, the landscape patterns of Hangzhou have undergone significant changes (Fig. 3), primarily manifested in the substitution of built-up areas from GS2 (Fig. 4). In general, the LULC pattern and its changes in Hangzhou over the past two decades were the

results of the joint action of politics and the economy. At the beginning of this century, "General Urban Planning of Hangzhou City (2001–2020)" formulated by the Hangzhou municipal government determined the spatial development strategy of "urban expansion to the east, tourism expansion to the west, development along the river, and cross river development" (Hangzhou Municipal Government, 2019), which

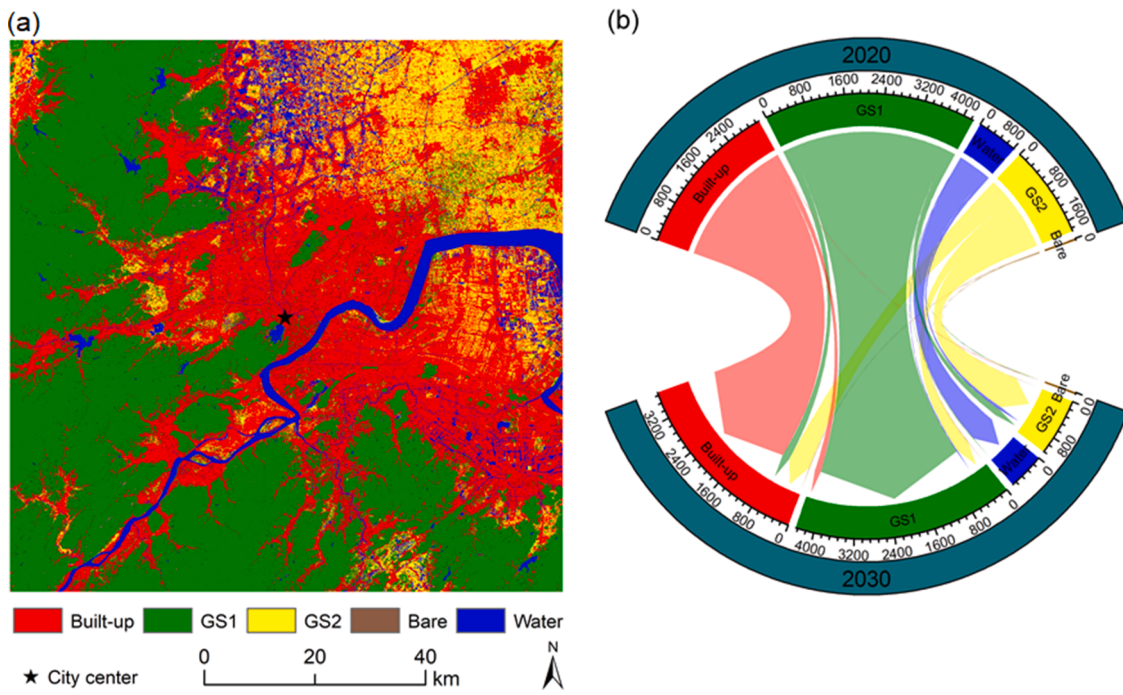


Fig. 7. Spatial and statistical characteristics of landscape patterns in 2030: (a) LULC distribution in 2030; and (b) LULC transition from 2020 to 2030 (in km^2).

had far-reaching impacts on the urban land pattern of Hangzhou. To host the Group of Twenty (G20) summit in 2016, Hangzhou underwent upgrading and transformation. After hosting the G20 summit, Hangzhou gained a new development opportunity. Coupled with the fact that it is the host city of the 2022 Asian Games, Hangzhou's demand for construction land has increased further. This is related to the observation that the increase in built-up areas and the reduction of GS2 in the second decade were more drastic than in the first decade (Fig. 4). The variation of LULC is the predominant controlling factor of urban high temperatures because it changes the land surface energy balance. Comparing Fig. 3 with Fig. 5, we detected that the pattern of LST was consistent with that of LULC. Similar to the research results of Hou and Estoque (2020) and Lin et al. (2018) in Hangzhou, the built-up area with a high albedo and small specific heat capacity had the highest LST, and the water with low albedo and large specific heat capacity had the lowest LST, indicating that water has a potential cooling effect.

Choosing an appropriate method or model is the key to accurately predicting the future SUHI. Traditional global and regional models are often at coarse resolution, which determines that they are not suitable for understanding local phenomena (Mushore et al., 2017). In the previous research on SUHI prediction, the MLR model was widely used to identify the key variables affecting SUHI (Oukawa et al., 2022). Once the relationship between the dependent and independent variables is determined, MLR can be applied for the prediction. However, the MLR has its limitation; that is, it cannot sufficiently represent the non-linear relationships between variables. In contrast, RF can deal with non-linear relations, which makes up for the weakness of MLR. Therefore, we compared the prediction ability of SMLR and RF models. Our research results showed RF models performed considerably better than the MLR models for all accuracy evaluation indexes, with higher R^2 and lower RMSE. Comparison studies conducted by Yao et al. (2021) in Meihekou (China) and Oukawa et al. (2022) in Londrina (Brazil) also found that the prediction accuracy of RF was significantly improved compared with linear regression when predicting UHI. However, since the RF model is a black box, it is difficult to understand how predictors are used to predict and mitigate SUHII (Gardes et al., 2020). Thus, it is necessary to use SMLR models to determine the relationship between landscape pattern and SUHII, and to provide an operational landscape optimization

scheme for actual SUHII mitigation work.

The correlation between landscape patterns and SUHII has obvious scale characteristics. In this context, determining the appropriate grid-scale is another key to predicting future SUHII. In contrast to most previous studies, this study conducted a multi-scale simulation of the SUHII pattern of Hangzhou in 2030 based on the RF models. In general, an increase in the spatial scale means a decline in spatial accuracy. The spatial accuracy of the 50×50 grid simulation results was less than that of the 17×17 and 33×33 grids, which indicates that the results might not be precise enough for a local-sized urban micro transformation. Considering the practical needs of urban planners, the grid size has not been further increased to pursue a potentially higher R^2 of the regression results. In addition, because the grid is relatively large and the SUHII within the grid is the mean SUHII, some potential high SUHII regions may be averaged. Therefore, in SUHII simulation, a trade-off between spatial scale and spatial precision should be determined according to the research needs.

Accurate simulation of future LULC patterns is crucial for precisely projecting the spatial distribution of future SUHII. Our simulation followed the law of LULC variation in Hangzhou from 2000 to 2020. By 2030, the built-up area is expected to reach 3740.67 km^2 , while GS2 is estimated to be reduced to 1130.96 km^2 . Suppose the expansion of built-up areas is not reasonably limited. In that case, the LULC structure of Hangzhou will face an imbalance, which will further lead to a decline in the regional ecosystem service function. Based on the modelling results of RF, SUHII was predicted to increase due to urban growth between 2020 and 2030, which agrees with already observed warming trends in Hangzhou (Lin et al., 2018; Tian et al., 2021; Wu et al., 2022). The region with SUHII greater than 5°C was primarily covered by built-up area, and its ruling area expanded with the expansion of the built-up area (Fig. 8). The growth of the built-up area was realised by replacing the surrounding GS2 region, which is one of the main land use types at the $0-2.5^\circ\text{C}$ level. Therefore, a large number of $0-2.5^\circ\text{C}$ areas are transformed into $>5^\circ\text{C}$ areas (Fig. 9b). The development pattern of outward expansion and inward agglomeration of the built-up area promoted the spatial connection and integration of the original scattered high-intensity heat island patches and new high-intensity heat island patches in the study area, forming a more concentrated and larger

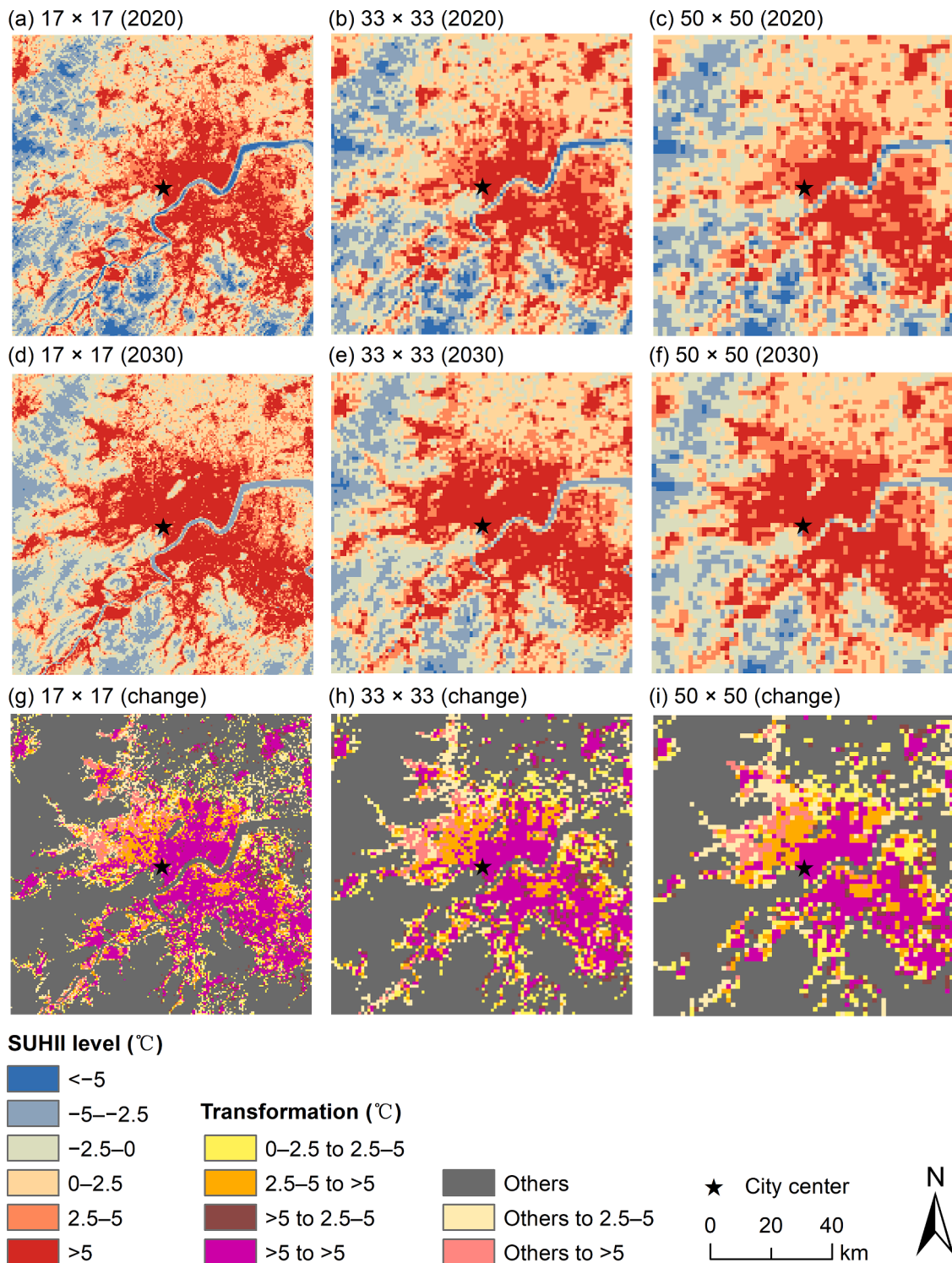


Fig. 8. Distribution maps of SUHII in Hangzhou: (a)–(c) are the SUHII distributions of the three grid scales (17×17 , 33×33 , and 50×50) in 2020; (d)–(f) are the SUHII distributions of the three grid scales in 2030; and (g)–(i) are the change maps of the three grid scales between 2000 and 2020.

coverage high-intensity heat island area. This evidence indicated that under the trend of urban expansion, the risk of SUHI in Hangzhou would further intensify, and more regions and populations would be threatened by high temperatures.

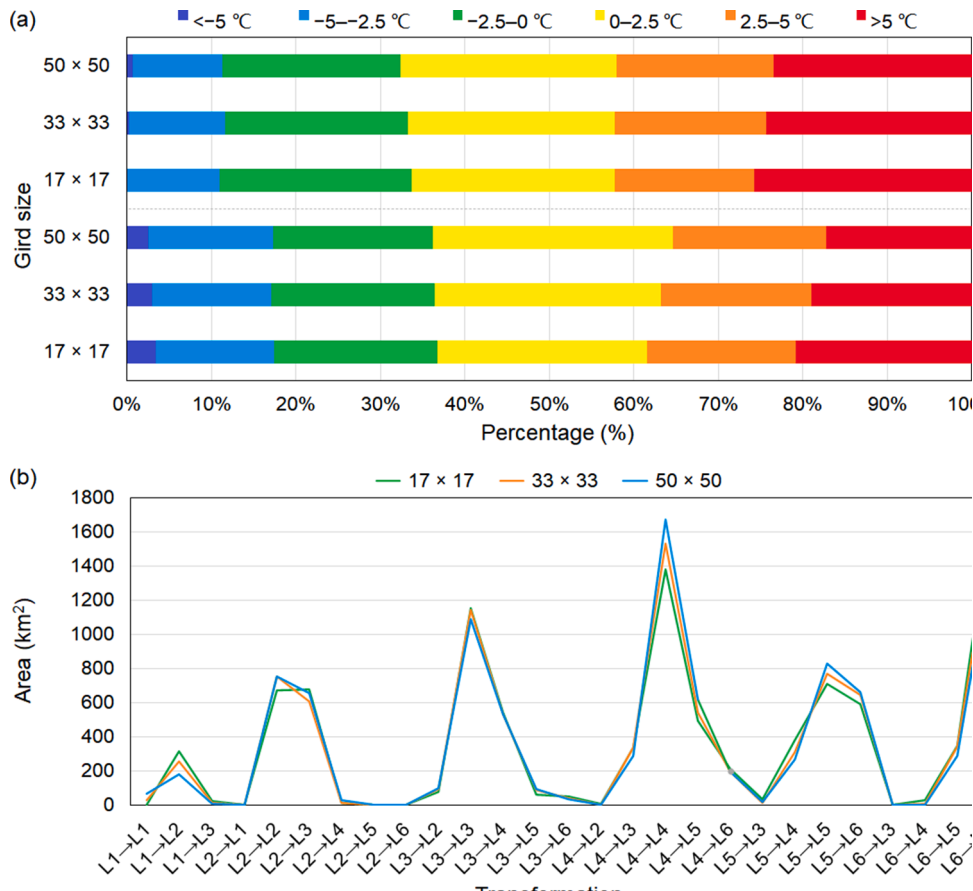
From the perspective of landscape composition, the fundamental method for alleviating UHI is reducing the built-up area and increasing the area of GS1, water, and GS2. However, in the context of rapid urbanization, it is unrealistic to reduce built-up areas significantly (Wang

et al., 2020). The trend of urbanization is irresistible, but the boundary of urban development can be controlled (Jiang et al., 2016). In future urban planning, decision-makers can control urban sprawl by delineating the boundaries of urban development. Although the effect of landscape configuration on LST is lower than that of landscape composition (Du et al., 2016), it is still an optimal way to improve the urban thermal environment considering its lower land command. Adjusting the configuration of each type of landscape is an effective way

Table 5

Statistics of each SUHII level in 2020 and 2030.

Size	510 m × 510 m (17 × 17)			990 m × 990 m (33 × 33)			1500 m × 1500 m (50 × 50)		
	Year	2020(km ²)	2030(km ²)	Net change(km ²)	2020(km ²)	2030(km ²)	Net change(km ²)	2020(km ²)	2030(km ²)
Category									
<−5 °C	341.86	0.78	−341.08	298.93	31.36	−267.57	256.50	67.50	−189.00
−5–−2.5 °C	1369.06	1075.15	−293.91	1380.96	1110.45	−270.51	1440.00	1044.00	−396.00
−2.5–0 °C	1889.01	2229.13	340.12	1894.53	2118.98	224.44	1851.75	2063.25	211.50
0–2.5 °C	2435.82	2353.59	−82.24	2614.91	2396.34	−218.56	2785.50	2502.00	−283.50
2.5–5 °C	1717.98	1621.71	−96.27	1747.52	1753.40	5.88	1775.25	1829.25	54.00
>5 °C	2047.26	2520.64	473.38	1864.15	2390.46	526.31	1692.00	2295.00	603.00

**Fig. 9.** Change detection of SUHII from 2020 to 2030: (a) The statistics of the area proportional to each SUHII level, and (b) the conversion area statistics for each SUHII level (L1: <−5 °C; L2: −5–−2.5 °C; L3: −2.5–0 °C; L4: 0–2.5 °C; L5: 2.5–5 °C; L6: >5 °C).

to reduce UHI. In this context, we propose the following recommendations to mitigate SUHI based on the regression results: (1) decrease the concentration and the PLAND of built-up areas; (2) reduce the aggregation and fragmentation of GS1; and (3) increase the concentration of GS2 and make its shape more complex. Although the proportions of water and bare were relatively low, modifications are still required. Scattered and low-density bare land and concentrated water are effective in reducing the SUHI.

Limitations and future prospects should be addressed for a better understanding of this study. First, LULC simulation is a complicated dynamic process. Given data restrictions, only socio-economic and natural terrain factors were considered in the LCM. For the purpose of enhancing reliability and certainty, more restrictive factors representing policy and anthropology are suggested to be included in future research. Moreover, the relationship between the landscape indices and SUHII changed with the grid size. In future studies, more grid sizes with smaller intervals are suggested to be tested to determine the optimal grid size for

each study area. Finally, the prediction of SUHII was based solely on the correlation between LULC and SUHII. Other factors, such as morphological information and preservation, should be considered to increase the accuracy of the results in future studies.

5. Conclusions

Predicting future UHI distribution aids in deepening the understanding of the future UHI characteristics based on current urban development. In addition, it is important to evaluate whether the current urban planning can support sustainable urban development. Thus, our research aimed to predict the future SUHI intensity and distribution based on landscape composition and configuration in Hangzhou in 2030. The comparison between SMLR and RF models indicated that the RF model was more helpful in realizing the accurate prediction of SUHII with higher R^2 (0.837) and lower RMSE (0.059). Future SUHII prediction results demonstrated that due to urban sprawl and agglomeration,

the SUHI effect in Hangzhou will be enhanced significantly in 2030. In order to reduce the high-temperature risk, according to the regression results of the landscape index and SUHII, we suggest that the urban landscape pattern should be further optimized, including arranging built-up areas and GS1 more scattered and fragmented and arranging GS2 more concentrated and irregular. In addition, in exploring the optimal prediction grid scale, we found that a grid of 50×50 with the highest fitting degree ($R^2 = 0.837$) is more realistic, but there are limitations in its spatial accuracy. Therefore, it is necessary to balance the spatial accuracy and scale according to the research purpose in future research.

In summary, this study provides a standard approach to evaluating the SUHI risk in the future based on predicted landscape patterns. The combination of the linear regression model and non-linear machine learning model in detecting the relationship between SUHII and landscape patterns ensures both the high accuracy and practicability of the results. Our findings detected the high-risk areas of SUHI in Hangzhou in 2030 based on random forest modelling. In addition, with the support of a stepwise multiple linear regression model, direct urban planning suggestions are proposed based on the relationships between SUHII and landscape composition and configuration. This whole process is recommended to be carried out in other cities that are facing urban thermal issues in summer. With the increase in available data, future studies are suggested to include 3-dimensional data to produce more comprehensive results.

Declaration of Competing Interest

The authors declare that they have no known competing financial interests or personal relationships that could have appeared to influence the work reported in this paper.

Acknowledgment

This study was funded by the Natural Science Foundation of Zhejiang Province (Grant Number: LQ20D010008; Representative: Hao Hou). The authors thank the editor-in-chief and anonymous reviewers for their constructive comments.

Supplementary materials

Supplementary material associated with this article can be found, in the online version, at doi:[10.1016/j.scs.2022.103992](https://doi.org/10.1016/j.scs.2022.103992).

References

- Ansari, A., & Golabi, M. H. (2019). Prediction of spatial land use changes based on LCM in a GIS environment for Desert Wetlands – A case study: Meighan Wetland, Iran. *International Soil and Water Conservation Research*, 7, 64–70. <https://doi.org/10.1016/j.iiswcr.2018.10.001>
- Bokaei, M., Zarkesh, M. K., Arasteh, P. D., & Hosseini, A. (2016). Assessment of urban heat island based on the relationship between land surface temperature and land use/land cover in Tehran. *Sustainable Cities and Society*, 23, 94–104. <https://doi.org/10.1016/j.scs.2016.03.009>
- Breiman, L. (2001). Random forests. *Machine Learning*, 45, 5–32. <https://doi.org/10.1023/A:1010933404324>
- Chanapathi, T., & Chanapathi, S. (2020). Investigating the impact of climate and land-use land cover changes on hydrological predictions over the Krishna river basin under present and future scenarios. *Science of The Total Environment*, 721, Article 137736. <https://doi.org/10.1016/j.scitotenv.2020.137736>
- Chen, D., Zhang, F., Zhang, M., Meng, Q., Jim, C. Y., Shi, J., Tan, M. L., & Ma, X. (2022). Landscape and vegetation traits of urban green space can predict local surface temperature. *Science of The Total Environment*, 825, Article 154006. <https://doi.org/10.1016/j.scitotenv.2022.154006>
- Das, M., & Das, A. (2019). Dynamics of urbanization and its impact on urban ecosystem services (UESs): A study of a medium size town of West Bengal, Eastern India. *Journal of Urban Management*, 8, 420–434. <https://doi.org/10.1016/j.jum.2019.03.002>
- Deng, C., & Wu, C. (2013). Examining the impacts of urban biophysical compositions on surface urban heat island: A spectral unmixing and thermal mixing approach. *Remote Sensing of Environment*, 131, 262–274. <https://doi.org/10.1016/j.rse.2012.12.020>
- Du, H., Wang, D., Wang, Y., Zhao, X., Qin, F., Jiang, H., & Cai, Y. (2016). Influences of land cover types, meteorological conditions, anthropogenic heat and urban area on surface urban heat island in the Yangtze River Delta Urban Agglomeration. *Science of The Total Environment*, 571, 461–470. <https://doi.org/10.1016/j.scitotenv.2016.07.012>
- Du, S., Xiong, Z., Wang, Y.-C., & Guo, L. (2016). Quantifying the multilevel effects of landscape composition and configuration on land surface temperature. *Remote Sensing of Environment*, 178, 84–92. <https://doi.org/10.1016/j.rse.2016.02.063>
- Esha, E. J., & Rahman, Md. T. U. (2021). Simulation of future land surface temperature under the scenario of climate change using remote sensing & GIS techniques of northwestern Rajshahi district, Bangladesh. *Environmental Challenges*, 5, Article 100365. <https://doi.org/10.1016/j.envc.2021.100365>
- Estoque, R. C., Murayama, Y., & Myint, S. W. (2017). Effects of landscape composition and pattern on land surface temperature: An urban heat island study in the megacities of Southeast Asia. *Science of The Total Environment*, 577, 349–359. <https://doi.org/10.1016/j.scitotenv.2016.10.195>
- Ezimadi, K., Chahardoli, M., Azadbakht, M., & Matkan, A. A. (2021). Spatiotemporal analysis of land surface temperature using multi-temporal and multi-sensor image fusion techniques. *Sustainable Cities and Society*, 64, Article 102508. <https://doi.org/10.1016/j.scs.2020.102508>
- Feng, Y., Li, H., Tong, X., Chen, L., & Liu, Y. (2018). Projection of land surface temperature considering the effects of future land change in the Taihu Lake Basin of China. *Global and Planetary Change*, 167, 24–34. <https://doi.org/10.1016/j.gloplacha.2018.05.007>
- Fitria, R., Kim, D., Baik, J., & Choi, M. (2019). Impact of biophysical mechanisms on urban heat island associated with climate variation and urban morphology. *Scientific Reports*, 9, 19503. <https://doi.org/10.1038/s41598-019-55847-8>
- Foley, J. A., DeFries, R., Asner, G. P., Barford, C., Bonan, G., Carpenter, S. R., Chapin, F. S., Coe, M. T., Daily, G. C., Gibbs, H. K., Helkowski, J. H., Holloway, T., Howard, E. A., Kucharik, C. J., Monfreda, C., Patz, J. A., Prentice, I. C., Ramankutty, N., & Snyder, P. K. (2005). Global consequences of land use. *Science*, 309, 570–574. <https://doi.org/10.1126/science.1111772>
- Fu, P., & Weng, Q. (2016). A time series analysis of urbanization induced land use and land cover change and its impact on land surface temperature with Landsat imagery. *Remote Sensing of Environment*, 175, 205–214. <https://doi.org/10.1016/j.rse.2015.12.040>
- Gardes, T., Schoetter, R., Hidalgo, J., Long, N., Marquès, E., & Masson, V. (2020). Statistical prediction of the nocturnal urban heat island intensity based on urban morphology and geographical factors—An investigation based on numerical model results for a large ensemble of French cities. *Science of The Total Environment*, 737, Article 139253.
- Grimm, N. B., Faeth, S. H., Golubiewski, N. E., Redman, C. L., Wu, J., Bai, X., & Briggs, J. M. (2008). Global change and the ecology of cities. *Science*, 319, 756–760. <https://doi.org/10.1126/science.1150195>
- Guo, A., Yang, J., Xiao, X., Xia (Cecilia), J., Jin, C., & Li, X. (2020). Influences of urban spatial form on urban heat island effects at the community level in China. *Sustainable Cities and Society*, 53, Article 101972. <https://doi.org/10.1016/j.scs.2019.101972>
- Hangzhou Municipal Bureau of Statistics. (2021). *Economic operation of Hangzhou in 2020*. http://tj.hangzhou.gov.cn/art/2021/1/29/art_1229279240_3840842.html (accessed 20 November 2021).
- Hangzhou Municipal Government. (2019). *General urban planning of Hangzhou City (2001–2020)*. http://ghzy.hangzhou.gov.cn/art/2019/10/31/art_1228962781_39671549.html (accessed 20 November 2021).
- Hangzhou Municipal Government. (2021). *The seventh census data of Hangzhou City*. http://www.hangzhou.gov.cn/art/2021/5/17/art_1229063404_3872501.html (accessed 20 November 2021).
- Henderson, J. V. (2010). Cities and development. *Journal of Regional Science*, 50, 515–540. <https://doi.org/10.1111/j.1467-9787.2009.00636.x>
- Hogan, M. A., Yamamoto, S., & Covell, D. F. (1970). Multiple linear regression analysis of scintillation gamma-ray spectra: Automatic candidate selection. *Nuclear Instruments and Methods*, 80, 61–68. [https://doi.org/10.1016/0029-554X\(70\)90298-3](https://doi.org/10.1016/0029-554X(70)90298-3)
- Hou, H., & Estoque, R. C. (2020). Detecting cooling effect of landscape from composition and configuration: An urban heat island study on Hangzhou. *Urban Forestry & Urban Greening*, 53, Article 126719. <https://doi.org/10.1016/j.ufug.2020.126719>
- Hou, H., Wang, R., & Murayama, Y. (2019). Scenario-based modelling for urban sustainability focusing on changes in cropland under rapid urbanization: A case study of Hangzhou from 1990 to 2035. *Science of The Total Environment*, 661, 422–431. <https://doi.org/10.1016/j.scitotenv.2019.01.208>
- Islam, K., Rahman, Md. F., & Jashimuddin, M. (2018). Modelling land use change using cellular automata and artificial neural network: The case of Chunati Wildlife Sanctuary, Bangladesh. *Ecological Indicators*, 88, 439–453. <https://doi.org/10.1016/j.ecolind.2018.01.047>
- Jiang, P., Cheng, Q., Gong, Y., Wang, L., Zhang, Y., Cheng, L., Li, M., Lu, J., Duan, Y., Huang, Q., & Chen, D. (2016). Using urban development boundaries to constrain uncontrolled urban sprawl in China. *Annals of the American Association of Geographers*, 106, 1321–1343. <https://doi.org/10.1080/24694452.2016.1198213>
- Kafy, A. A., Rahman, Md. S., Faisal, A. A., Hasan, M. M., & Islam, M. (2020). Modelling future land use land cover changes and their impacts on land surface temperatures in Rajshahi, Bangladesh. *Remote Sensing Applications: Society and Environment*, 18, Article 100314. <https://doi.org/10.1016/j.rsase.2020.100314>
- Kalnay, E., & Cai, M. (2003). Impact of urbanization and land-use change on climate. *Nature*, 423, 528–531. <https://doi.org/10.1038/nature01675>
- Kang, P., Chen, W., Hou, Y., & Li, Y. (2019). Spatial-temporal risk assessment of urbanization impacts on ecosystem services based on pressure-status—Response framework. *Scientific Reports*, 9, 16806. <https://doi.org/10.1038/s41598-019-52719-z>

- Khan, M., Tahir, A. A., Ullah, S., Khan, R., Ahmad, K., Shahid, S. U., & Nazir, A. (2022). Trends and projections of land use land cover and land surface temperature using an integrated weighted evidence-cellular automata (WE-CA) model. *Environmental Monitoring and Assessment*, 194, 120. <https://doi.org/10.1007/s10661-022-09785-0>
- Kindu, M., Schneider, T., Teketay, D., & Knoke, T. (2016). Changes of ecosystem service values in response to land use/land cover dynamics in Munessa-Shashemene landscape of the Ethiopian highlands. *Science of The Total Environment*, 547, 137–147. <https://doi.org/10.1016/j.scitotenv.2015.12.127>
- Leta, M. K., Demissie, T. A., & Tränckner, J. (2021). Modelling and prediction of land use land cover change dynamics based on land change modeler (LCM) in Nashe Watershed, Upper Blue Nile Basin, Ethiopia. *Sustainability*, 13, 3740. <https://doi.org/10.3390/su13073740>
- Li, H., Meier, F., Lee, X., Chakraborty, T., Liu, J., Schaap, M., & Sodoudi, S. (2018). Interaction between urban heat island and urban pollution island during summer in Berlin. *Science of The Total Environment*, 636, 818–828. <https://doi.org/10.1016/j.scitotenv.2018.04.254>
- Lin, Y., Jim, C. Y., Deng, J., & Wang, Z. (2018). Urbanization effect on spatiotemporal thermal patterns and changes in Hangzhou (China). *Building and Environment*, 145, 166–176. <https://doi.org/10.1016/j.buildenv.2018.09.020>
- Liú, C., Zhang, F., Carl Johnson, V., Duan, P., & Kong, H. (2021). Spatio-temporal variation of oasis landscape pattern in arid area: Human or natural driving? *Ecological Indicators*, 125, Article 107495. <https://doi.org/10.1016/j.ecolind.2021.107495>
- Liú, H., Huang, B., Zhan, Q., Gao, S., Li, R., & Fan, Z. (2021). The influence of urban form on surface urban heat island and its planning implications: Evidence from 1288 urban clusters in China. *Sustainable Cities and Society*, 71, Article 102987. <https://doi.org/10.1016/j.scs.2021.102987>
- Liú, X., Liang, X., Li, X., Xu, X., Ou, J., Chen, Y., Li, S., Wang, S., & Pei, F. (2017). A future land use simulation model (FLUS) for simulating multiple land use scenarios by coupling human and natural effects. *Landscape and Urban Planning*, 168, 94–116. <https://doi.org/10.1016/j.landurbplan.2017.09.019>
- Lu, H., Li, F., Yang, G., & Sun, W. (2021). Multi-scale impacts of 2D/3D urban building pattern in intra-annual thermal environment of Hangzhou, China. *International Journal of Applied Earth Observation and Geoinformation*, 104, Article 102558. <https://doi.org/10.1016/j.jag.2021.102558>
- Maimaitiyiming, M., Ghulam, A., Tiyip, T., Pla, F., Latorre-Carmona, P., Halik, Ü., Sawut, M., & Caetano, M. (2014). Effects of green space spatial pattern on land surface temperature: Implications for sustainable urban planning and climate change adaptation. *ISPRS Journal of Photogrammetry and Remote Sensing*, 89, 59–66. <https://doi.org/10.1016/j.isprsjprs.2013.12.010>
- Manoli, G., Fatichi, S., Schläpfer, M., Yu, K., Crowther, T. W., Meili, N., Burlando, P., Katul, G. G., & Bou-Zeid, E. (2019). Magnitude of urban heat islands largely explained by climate and population. *Nature*, 573, 55–60. <https://doi.org/10.1038/s41586-019-1512-9>
- McGarigal, K., Cushman, S., & Ene, E. (2012). FRAGSTATS: Spatial pattern analysis program for categorical maps. <http://www.umass.edu/landeco/research/fragstats/fragstats.html> (accessed 12 February 2022).
- Meng, Q., Zhang, L., Sun, Z., Meng, F., Wang, L., & Sun, Y. (2018). Characterizing spatial and temporal trends of surface urban heat island effect in an urban main built-up area: A 12-year case study in Beijing, China. *Remote Sensing of Environment*, 204, 826–837. <https://doi.org/10.1016/j.rse.2017.09.019>
- Mohammad Harmay, N. S., Kim, D., & Choi, M. (2021). Urban heat island associated with land use/land cover and climate variations in Melbourne, Australia. *Sustainable Cities and Society*, 69, Article 102861. <https://doi.org/10.1016/j.scs.2021.102861>
- Mushore, T. D., Odindi, J., Dube, T., & Mutanga, O. (2017). Prediction of future urban surface temperatures using medium resolution satellite data in Harare metropolitan city, Zimbabwe. *Building and Environment*, 122, 397–410. <https://doi.org/10.1016/j.buildenv.2017.06.033>
- Nadizadeh Shorabeh, S., Hamzeh, S., Zanganeh Shahraki, S., Firozjaei, M. K., & Jokar Arsanjani, J. (2020). Modelling the intensity of surface urban heat island and predicting the emerging patterns: Landsat multi-temporal images and Tehran as case study. *International Journal of Remote Sensing*, 41, 7400–7426. <https://doi.org/10.1080/01431161.2020.1759841>
- Oukawa, G. Y., Krecl, P., & Targino, A. C. (2022). Fine-scale modelling of the urban heat island: A comparison of multiple linear regression and random forest approaches. *Science of The Total Environment*, 815, Article 152836. <https://doi.org/10.1016/j.scitotenv.2021.152836>
- Pal, S., & Ziaul, Sk (2017). Detection of land use and land cover change and land surface temperature in English Bazar urban centre. *The Egyptian Journal of Remote Sensing and Space Science*, 20, 125–145. <https://doi.org/10.1016/j.ejrs.2016.11.003>
- Peng, J., Hu, Y., Dong, J., Liu, Q., & Liu, Y. (2020). Quantifying spatial morphology and connectivity of urban heat islands in a megacity: A radius approach. *Science of The Total Environment*, 714, Article 136792. <https://doi.org/10.1016/j.scitotenv.2020.136792>
- Peng, J., Xie, P., Liu, Y., & Ma, J. (2016). Urban thermal environment dynamics and associated landscape pattern factors: A case study in the Beijing metropolitan region. *Remote Sensing of Environment*, 173, 145–155. <https://doi.org/10.1016/j.rse.2015.11.027>
- Pontius, R. G., Boersma, W., Castella, J.-C., Clarke, K., de Nijs, T., Dietzel, C., Duan, Z., Fotsing, E., Goldstein, N., Kok, K., Koomen, E., Lippitt, C. D., McConnell, W., Mohd Sood, A., Pijanowski, B., Pithadia, S., Sweeney, S., Trung, T. N., Veldkamp, A. T., & Verburg, P. H. (2008). Comparing the input, output, and validation maps for several models of land change. *The Annals of Regional Science*, 42, 11–37. <https://doi.org/10.1007/s00168-007-0138-2>
- Rahman, M., Ningsheng, C., Mahmud, G. I., Islam, M. M., Pourghasemi, H. R., Ahmad, H., Habumugisha, J. M., Washakh, R. M. A., Alam, M., Liu, E., Han, Z.,
- Ni, H., Shufeng, T., & Dewan, A. (2021). Flooding and its relationship with land cover change, population growth, and road density. *Geoscience Frontiers*, 12, Article 101224. <https://doi.org/10.1016/j.gsf.2021.101224>
- Sharma, S., Nahid, S., Sharma, M., Sannigrahi, S., Anees, M. M., Sharma, R., Shekhar, R., Basu, A. S., Pilla, F., Basu, B., & Joshi, P. K. (2020). A long-term and comprehensive assessment of urbanization-induced impacts on ecosystem services in the capital city of India. *City and Environment Interactions*, 7, Article 100047. <https://doi.org/10.1016/j.cacint.2020.100047>
- Shi, Y., Liu, S., Yan, W., Zhao, S., Ning, Y., Peng, X., Chen, W., Chen, L., Hu, X., Fu, B., Kennedy, R., Lv, Y., Liao, J., Peng, C., Rosa, I. M. D., Roy, D., Shen, S., Smith, A., Wang, C., Wang, Z., Xiao, L., Xiao, J., Yang, L., Yuan, W., Yi, M., Zhang, H., Zhao, M., & Zhu, Y. (2021). Influence of landscape features on urban land surface temperature: Scale and neighborhood effects. *Science of The Total Environment*, 771, Article 145381. <https://doi.org/10.1016/j.scitotenv.2021.145381>
- Sloan, S., & Pelletier, J. (2012). How accurately may we project tropical forest-cover change? A validation of a forward-looking baseline for REDD. *Global Environmental Change*, 22, 440–453. <https://doi.org/10.1016/j.gloenvcha.2012.02.001>
- Song, X.-P., Hansen, M. C., Stehman, S. V., Potapov, P. V., Tyukavina, A., Vermote, E. F., & Townshend, J. R. (2018). Global land change from 1982 to 2016. *Nature*, 560, 639–643. <https://doi.org/10.1038/s41586-018-0411-9>
- Sun, L., Chen, J., Li, Q., & Huang, D. (2020). Dramatic uneven urbanization of large cities throughout the world in recent decades. *Nature Communications*, 11, 5366. <https://doi.org/10.1038/s41467-020-19158-1>
- Tariq, A., & Shu, H. (2020). CA-Markov chain analysis of seasonal land surface temperature and land use land cover change using optical multi-temporal satellite data of Faisalabad, Pakistan. *Remote Sensing*, 12, 3402. <https://doi.org/10.3390/rs12203402>
- Tian, P., Li, J., Cao, L., Pu, R., Wang, Z., Zhang, H., Chen, H., & Gong, H. (2021). Assessing spatiotemporal characteristics of urban heat islands from the perspective of an urban expansion and green infrastructure. *Sustainable Cities and Society*, 74, Article 103208. <https://doi.org/10.1016/j.scs.2021.103208>
- Ullah, Tahir, Akbar, Hassan, Dewan, Khan, & Khan. (2019). Remote sensing-based quantification of the relationships between land use land cover changes and surface temperature over the Lower Himalayan Region. *Sustainability*, 11, 5492. <https://doi.org/10.3390/su11195492>
- Unal Cilek, M., & Cilek, A. (2021). Analyses of land surface temperature (LST) variability among local climate zones (LCZs) comparing Landsat-8 and ENVI-met model data. *Sustainable Cities and Society*, 69, Article 102877. <https://doi.org/10.1016/j.scs.2021.102877>
- United Nation. (2020). *World cities report 2020*. <https://unhabitat.org/World%20Cities%20Report%202020> (accessed 6 March 2022).
- Wang, L., Hou, H., & Weng, J. (2020). Ordinary least squares modelling of urban heat island intensity based on landscape composition and configuration: A comparative study among three megacities along the Yangtze River. *Sustainable Cities and Society*, 62, Article 102381. <https://doi.org/10.1016/j.scs.2020.102381>
- Wang, R., Hou, H., Murayama, Y., & Derdouri, A. (2020). Spatiotemporal analysis of land use/cover patterns and their relationship with land surface temperature in Nanjing, China. *Remote Sensing*, 12, 440. <https://doi.org/10.3390/rs12030440>
- Wang, R., & Murayama, Y. (2020). Geo-simulation of land use/cover scenarios and impacts on land surface temperature in Sapporo, Japan. *Sustainable Cities and Society*, 63, Article 102432. <https://doi.org/10.1016/j.scs.2020.102432>
- Wang, Z., Meng, Q., Allam, M., Hu, D., Zhang, L., & Menenti, M. (2021). Environmental and anthropogenic drivers of surface urban heat island intensity: A case-study in the Yangtze River Delta, China. *Ecological Indicators*, 128, Article 107845. <https://doi.org/10.1016/j.ecolind.2021.107845>
- Wu, H., Ye, L.-P., Shi, W.-Z., & Clarke, K. C. (2014). Assessing the effects of land use spatial structure on urban heat islands using HJ-1B remote sensing imagery in Wuhan, China. *International Journal of Applied Earth Observation and Geoinformation*, 32, 67–78. <https://doi.org/10.1016/j.jag.2014.03.019>
- Wu, Y., Hou, H., Wang, R., Murayama, Y., Wang, L., & Hu, T. (2022). Effects of landscape patterns on the morphological evolution of surface urban heat island in Hangzhou during 2000–2020. *Sustainable Cities and Society*, 79, Article 103717. <https://doi.org/10.1016/j.scs.2022.103717>
- Yang, C., Yan, F., Lei, X., Ding, X., Zheng, Y., Liu, L., & Zhang, S. (2020). Investigating seasonal effects of dominant driving factors on urban land surface temperature in a snow-climate city in China. *Remote Sensing*, 12, 3006. <https://doi.org/10.3390/rs12183006>
- Yao, Z., Jiafu, L., & Zhuyun, W. (2021). Predicting surface urban heat island in Meihekou City, China: A combination method of Monte Carlo and random forest. *Chinese Geographical Science*, 31, 12.
- Yin, C., Yuan, M., Lu, Y., Huang, Y., & Liu, Y. (2018). Effects of urban form on the urban heat island effect based on spatial regression model. *Science of The Total Environment*, 634, 696–704. <https://doi.org/10.1016/j.scitotenv.2018.03.350>
- Yohannes, H., Soromessa, T., Argaw, M., & Dewan, A. (2021). Spatio-temporal changes in habitat quality and linkage with landscape characteristics in the Beressa watershed, Blue Nile basin of Ethiopian highlands. *Journal of Environmental Management*, 281, Article 111885. <https://doi.org/10.1016/j.jenvman.2020.111885>
- Zhang, R. (2020). Cooling effect and control factors of common shrubs on the urban heat island effect in a southern city in China. *Scientific Reports*, 10, 17317. <https://doi.org/10.1038/s41598-020-74559-y>

- Zhao, J., Zhao, X., Liang, S., Zhou, T., Du, X., Xu, P., & Wu, D. (2020). Assessing the thermal contributions of urban land cover types. *Landscape and Urban Planning*, 204, Article 103927. <https://doi.org/10.1016/j.landurbplan.2020.103927>
- Zhao, L., Lee, X., Smith, R. B., & Oleson, K. (2014). Strong contributions of local background climate to urban heat islands. *Nature*, 511, 216–219. <https://doi.org/10.1038/nature13462>
- Zheng, Y., Li, Y., Hou, H., Murayama, Y., Wang, R., & Hu, T. (2021). Quantifying the cooling effect and scale of large inner-city lakes based on landscape patterns: A case study of Hangzhou and Nanjing. *Remote Sensing*, 13, 1526. <https://doi.org/10.3390/rs13081526>